galaxies

MDPI

Article

Probing the Dusty Torus of Seyfert Galaxy NGC 4151: A Multi-Band Study

Arya Sudhakaran [1], Debbijoy Bhattacharya [1,*], Puthiyaveettil Shalima [1], Gulab Chand Dewangan [2] and Parameshwaran Sreekumar [1]

[1] Manipal Centre for Natural Sciences, Manipal Academy of Higher Education, Manipal 576104, India; arya.mcnsmpl2022@learner.manipal.edu (A.S.); shalima.p@manipal.edu (P.S.); sreekumar.p@manipal.edu (P.S.)
[2] Inter-University Centre for Astronomy and Astrophysics (IUCAA), PB No.4, Ganeshkhind, Pune 411007, India; gulabd@iucaa.in
* Correspondence: debbijoy.b@manipal.edu

Abstract

Despite several efforts to investigate the accretion disk and torus, near-simultaneous broadband studies of the nuclear regions of radio-quiet AGNs remain lacking. NGC 4151, one of the closest and brightest Seyfert galaxies, provides an excellent laboratory for probing the circum-nuclear regions of AGNs. A detailed, near-simultaneous broadband spectral study of NGC 4151 is carried out during one of its historic minimum activity states, using archival data from the Ultraviolet (UV) to the Infrared (IR) regions. We used the radiative transfer code SKIRT to model the source and to constrain the properties of the torus. We found that the observed broadband spectral energy distribution is best explained by a two-torus geometry with a polar conical shell structure.

Keywords: galaxies: active; galaxies: nuclei; galaxies: Seyfert; radiative transfer

1. Introduction

Active Galactic Nuclei (AGNs) are highly luminous massive objects ($M_{BH} \sim 10^6$–$10^{10} M_\odot$) powered by the accretion of matter [1] onto supermassive black holes (SMBHs). In the vast majority of AGNs (∼80–90%), the ratio of radio flux at 5 GHz to the B band optical flux is observed to be less than 1 [2]. Such AGNs are called 'Radio-Quiet (RQ)'-AGNs. Seyfert galaxies are a subclass of RQ-AGNs characterized by moderate to low luminosity, with an absolute magnitude of $M_B > -23$ [3]. Seyfert galaxies, which exhibit both broad and narrow optical emission lines, are called Type-1 AGNs, whereas Type-2 AGNs show only narrow emission lines.

According to the RQ-AGN unification scheme [4,5], differences observed between the optical spectra of Type-1 and Type-2 Seyferts arise primarily due to the orientation of a "dusty torus" in the line of sight between the observer and the broad-line region (BLR). The Type-1 AGNs are viewed face-on; therefore, the emission from the BLR clouds can be directly observed, which explains the broad emission lines in their spectra. Conversely, an edge-on view intersects the torus, obscuring the BLR and nuclear regions of AGN, resulting in (Type-2) narrow emission lines.

Dust in the torus is expected to absorb a considerable fraction of the optical and UV radiation produced by the accretion disk, which is then reprocessed into IR radiation. For weak-jetted AGNs, the thermal radiation from dust grains in the torus is expected to be the prime source of emission in the IR energy bands [6]. Even more than thirty

Check for updates

Academic Editor: Bidzina Kapanadze

Received: 5 November 2025
Revised: 20 December 2025
Accepted: 24 December 2025
Published: 6 January 2026

Copyright: © 2026 by the authors. Licensee MDPI, Basel, Switzerland. This article is an open access article distributed under the terms and conditions of the Creative Commons Attribution (CC BY) license.

years after the proposition ([7], and the references therein), the geometry, composition, and other physical properties of the torus remain elusive. There have been many attempts to constrain the properties of the torus from observed optical and IR emission. Early analytical models employed simplistic structures, such as an annular ring/flared disk, with a two-dimensional uniform density distribution of dust surrounding the accretion disk [8,9]. However, even before these works, Krolik and Begelman [10] argued that a homogeneously distributed torus may not be physically possible, as the dust cannot survive near the central engine. Instead, they suggested that the dust is more likely to be clumpy or cloud-like. From mid-IR (MIR) interferometry observations, Jaffe et al. [11] reported spatially resolved structures in the dusty torus of NGC 1068, which supports the proposition by Krolik and Begelman [10].

Over the last two decades, radiative transfer (RT) modelling has been carried out to constrain the dust composition and geometry of the torus (e.g., [12–15]). Present day RT codes, such as CLUMPY [16,17], "Clumpy AGN Tori in a 3D geometry (CAT-3D)" [18], RADMC-3D [13], and "Stellar Kinematics including Radiative Transfer (SKIRT)" [14] are widely used to model dust emission in AGN, incorporating advanced geometry and dust distribution [17,19–24].

SKIRT provides a fully three-dimensional Monte Carlo RT framework with high flexibility, enabling the implementation of arbitrary dust geometries through a range of built-in structures and classes, together with adjustable smooth and clumpy dust mixtures. These capabilities are particularly well-suited for modelling complex torus configurations comprising multiple torus components.

NGC 4151 is one of the brightest nearby Seyfert galaxies (z = 0.0033; [25]) at a distance of ∼15.8 Mpc (megaparsecs) [26]. NGC 4151 was initially classified as a broad-line Seyfert [27]. Several studies have investigated the properties of the source across multiple wavebands [28–34]. Though originally classified as an RQ-AGN [35], later observations in radio, X-ray, and γ-ray bands indicate the presence of possible jet/outflow activity in NGC 4151 [36–41]. Recently, NGC 4151 has also been classified as a changing-look AGN, exhibiting both changing-state and changing-obscuration behavior [33,42]. Variations in the accretion rate are generally considered the primary driver of changing-state transitions [33] with higher accretion rates typically associated with Type-1 states and lower rates with Type-2 states, while changes in the line-of-sight obscuration can give rise to changing-obscuration events. The optical and UV variability of NGC 4151 has been well-studied over many decades (e.g., [43–46]). This is one of the few sources that includes extensive IR reverberation studies [47–49].

There have been several attempts to study the inner structure of this source using observations at different wavelengths, mainly in the IR, optical, and X-ray ranges (e.g., [28,32,50–53]). Alonso-Herrero et al. [54] investigated the torus properties of 13 nearby Seyfert galaxies by modelling their IR observations using the CLUMPY torus models. In the case of NGC 4151, the CLUMPY models showed significant discrepancies in the near-IR (NIR) regime (Figure 4 of [54]). Using SKIRT, Swain et al. [50] modelled the IR spectral energy distribution (SED) of NGC 4151 by considering an inner ring and an outer torus with a two-phase clumpy dust distribution. Although this model successfully reproduced the observed NIR excess, it failed to explain the mid-IR (MIR) emission of the source. Furthermore, to the best of our knowledge, previous torus modelling studies of NGC 4151 have largely relied on non-simultaneous IR observations, which is a significant limitation given the strong variability exhibited by NGC 4151 [20,53,55]. Previous studies, such as Cerqueira-Campos et al. [56], modelled SEDs using optical, NIR, and MIR photometry from Gaia, 2MASS, and WISE. Their analysis focused on the IR torus properties of Coronal-Line Forest AGNs, using NGC 4151 as a comparison object. However, their mod-

elling did not include UV observation. Marin et al. [57] constructed a broadband SED of NGC 4151 using polarized emission over a broad UV-IR waveband. However, they did not perform detailed RT modelling of the broadband SED. More recently, Kumar et al. [34] presented a temporally resolved study of NGC 4151, although their analysis was restricted to simultaneous UV-to-X-ray data.

A key limitation of most AGN torus studies is the lack of broadband coverage, as they are typically confined either to the IR–optical or UV–X-ray bands. In the case of NGC 4151, existing torus studies based on non-simultaneous IR data are further complicated by the strong variability exhibited by this source. AGN exhibits high flaring states as well as low activity states. To understand the underlying physical processes at work and the dynamics of the system, it is essential to study these sources in both their high and low activity states. However, most studies focus on the physical processes responsible for the high activity states, while investigations of AGNs during their low-activity phases remain limited (e.g., [58,59]).

In this work, we conducted a near-simultaneous broadband spectral study of NGC 4151 during one of its low activity states, utilising UV, optical, and IR wavelengths to constrain its torus properties. Section 2 describes the multi-band data used in this work. Section 3 presents the results of the 3D radiative transfer modelling, and Section 4 summarizes our main conclusions.

2. Data

The long-term UV light curve of NGC 4151 [34,46] is shown in Figure 1. A broadband SED of this source was constructed during the year 2000. The source was in a low-activity state during that period (shaded region in the Figure 1).

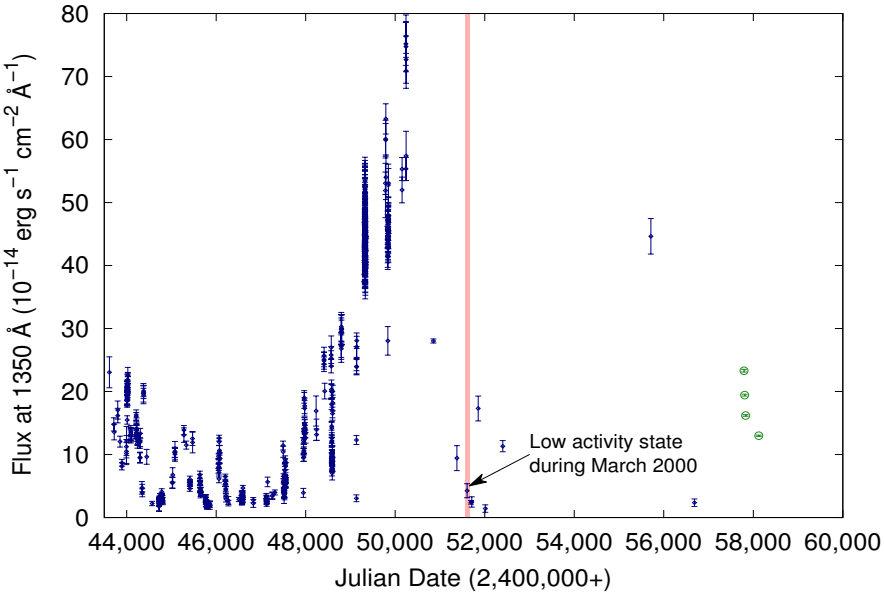


Figure 1. Far ultraviolet continuum light curve from 1976 to 2018. Observations from 1976 to 2014 are obtained from Couto et al. [46], Kraemer et al. [60], and the 2017–2018 data come from Astrosat UVIT observations as obtained from Kumar et al. [34]. Low activity states are identified here.

2.1. Optical & IR Data

Optical/IR photometric data are taken from Lyu and Rieke [61,62] and references therein). They presented a four-decade-long optical and IR light-curve (B, J, H, K, L bands). These data had already been corrected for aperture effects, galactic extinction, and host–galaxy contamination [62]. The B band has the best temporal coverage, and the NIR bands

have sparse data. In order to achieve a near-simultaneous broadband SED, for each band, the epoch of observation closest to the UV observation (3 March 2000) was considered.

Lyu and Rieke [62] suggest a nominal flux error of ∼5% when the AGN nucleus is in a bright state. However, the source was in a relatively low-flux state during 2000; therefore, the error could be much higher than ∼5%. To estimate the errors, we calculated the standard deviation σ of the flux values within a 90-day range centered on 3 March 2000. The flux uncertainty was then considered to be $\sigma/\sqrt{n}$, where n is the number of available observations within the time window. The calculated uncertainties in these optical to NIR bands (B, J, H, K, L) ranged from ∼5–13%. We adopted a conservative limit of 10% uncertainty across these bands. The 10 μm data for the source were obtained from Gorjian et al. [63]. The observations were carried out on 25 March 2000, using the MIR large-well imager (MIRLIN) on the Palomar telescope.

Non-simultaneous MIR data: Space-based MIR observations in the 20–40 μm range from Spitzer, WISE, and AKARI were discussed by Lyu and Rieke [62]. Although the available cadence is insufficient to draw strong conclusions about variability, the 24 μm flux measurements from Spitzer IRS, MIPS, and AKARI/IRC obtained at different epochs are consistent with each other within 3σ. Similarly, the fluxes at 34 μm and 37 μm show no significant evidence for variability across epochs. Therefore, we used the non-simultaneous MIR fluxes at 24, 34, and 37 μm as an independent consistency check on the model predictions rather than as direct constraints in the fitting procedure.

2.2. UV Data

The STIS/HST observed the source in a relatively low-UV flux state on 3 March 2000. For the construction of the simultaneous SED, we extracted the continuum flux at 1350 Å as obtained from the light curve presented in Kraemer et al. [60].

The light-travel distance across the torus in NGC 4151, on the order of several tens of days, can produce time offsets between the UV/optical and IR emission, potentially introducing uncertainties in the constructed SED. Using 36 years of observations, Lyu and Rieke [62] reported time delays of approximately ∼40 and ∼90 days between the optical and IR light curves. However, their analysis was limited by sparse cadence and gaps in the data. The available IR observations within 90 days of the UV/optical and X-ray epoch considered in our study are very limited. Therefore, we used the IR flux measurement closest in time to the UV epoch rather than an average IR flux. The near-simultaneous multi-wavelength data used in this work are summarized in Table 1.

Table 1. UV, Optical and Infrared observations during the low state. F_λ is the flux at wavelength λ.

λ (μm)	λF_λ (10^{-10} ergs cm^{-2} s^{-1})	Wavelength Band	Epoch	Reference
0.135	0.57 ± 0.15	G140M grating	3 March 2000	Kraemer et al. [60]
0.44	0.80 ± 0.08	B	4 March 2000	Lyu and Rieke [62]
1.22	0.67 ± 0.07	J	15 March 2000	Lyu and Rieke [62]
1.63	0.40 ± 0.04	H	6 April 2000	Lyu and Rieke [62]
2.19	1.12 ± 0.10	K	15 March 2000	Lyu and Rieke [62]
3.40	2.4 ± 0.24	L	15 March 2000	Lyu and Rieke [62]
10.0	5.6 ± 0.4	N	25 March 2000	Gorjian et al. [63]

3. Analysis & Results

A simultaneous broadband SED study of NGC 4151 is necessary to understand the geometry, composition, and morphology of the torus. However, to the best of our knowledge, no such study has been reported to date.

The near-simultaneous broadband SED of NGC 4151 was constructed using observations across different bands, selected to be as close as possible to the UV observation date of 3 March 2000. We used the RT code SKIRT version 9 [14,64] to model the dust around the AGN torus. The SKIRT code simultaneously handles the dust emission, dust absorption, and dust re-emission. Our primary objective is to constrain the torus properties utilising broadband SED that includes multiple IR bands. Therefore, inclusion of dust re-emission in the model is crucial. Hence, we restricted our SKIRT simulations within UV to IR ranges, where dust absorption and re-emission dominate.

The emission from the accretion disk surrounding the central SMBHs is generally regarded as the primary source that illuminates the torus. Therefore, its emission spectrum is considered an input to the SKIRT simulation. The choice of input AGN spectrum and various torus components used in the modelling are described below.

3.1. Input SED of Primary Source

There have been many efforts to construct the input SED (e.g., [9,17,18,20,65,66]). The radiative transfer code SKIRT also provides a default AGN primary source spectrum (*quasarSED*) [21]. These input SEDs are typically described by a combination of different power laws, with the slopes and wavelength boundaries varying across models. However, all such templates are based on average spectral properties derived from large AGN samples. Given the variable nature of AGN, the input SED for an individual source at a specific epoch is likely to deviate from these average representations.

Long-term UV observation suggests that the source is at its historic low state (Figure 1). We consider the source to be accreting at a 1% Eddington accretion rate. The mass of the central black hole is adopted as 1.7×10^7 $M_\odot$ [67], and we take the radiative efficiency (η) as 0.1. Under these assumptions, the value of the intrinsic bolometric luminosity (L_{Bol}) is 5.6×10^9 $L_\odot$, which better explains the observed SED. We assumed that the accretion disk emits as a multi-colour blackbody, modeling the accretion disk emission using the `diskbb` model of XSPEC. Most earlier works assumed isotropic emission from the accretion disk [17,65]. However, we considered anisotropic emission of the accretion disk as discussed by Stalevski et al. ([21], and references therein). Figure 2 shows the input SED for an inner disk temperature ($T_{\rm in}$) of 4 eV.

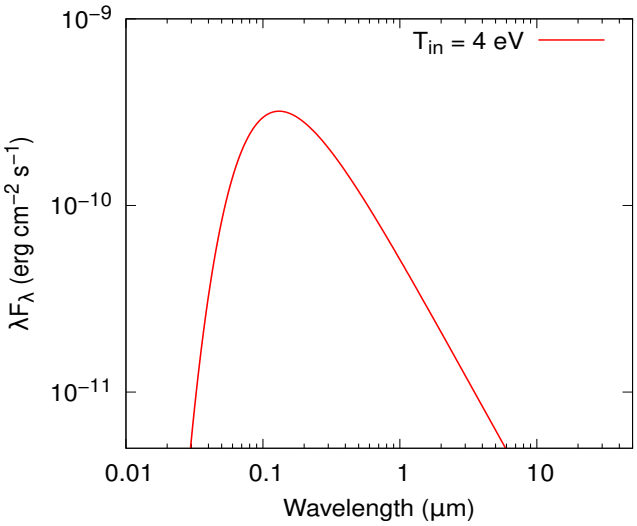


Figure 2. The primary source SED of NGC 4151 for $T_{\rm in} = 4$ eV.

3.2. Torus Geometry

The dust surrounding the central engine plays a crucial role in the observed SED. The UV/optical continuum radiation emitted by the accretion disc is absorbed and re-emitted by this dust in the IR regime. Hence, a more realistic torus geometry must be modelled to reproduce the observed SED.

We modelled the spatial dust distribution around the central engine as a three-component model, which includes (a) an inner torus with a flared disc geometry, (b) an outer torus with a flared disc geometry, and (c) a polar conical shell structure as shown in Figure 3. The inclusion of a polar conical shell component is motivated by the earlier works (e.g., [47,68–70]), where the presence of an extended mid-IR emission from the polar dust/wind was suggested in NGC 4151 and a few other Seyfert galaxies, which extends up to hundreds of parsecs.

These two equatorial tori with flared disc geometry are characterized by parameters such as half opening angle (σ), the inner radius ($R_{\rm in}$), and outer radius ($R_{\rm out}$). The parameters for the inner and outer tori are differentiated by using subscripts I and O, respectively. We considered the half opening angle (σ) of the inner and outer torus to be 23° [62], in agreement with 15–33° σ of the NLR bicone in NGC 4151 [71]. The schematic diagram of the adopted model is shown in Figure 4. For the inner radius ($R_{\rm in}$) of the inner torus, we adopted 0.04 pc as its value, in agreement with the SKIRT modeling of Swain et al. [50] and reverberation analysis of Lyu and Rieke [62], Minezaki et al. [72] and NIR long-baseline interferometric studies of Kishimoto et al. [73].

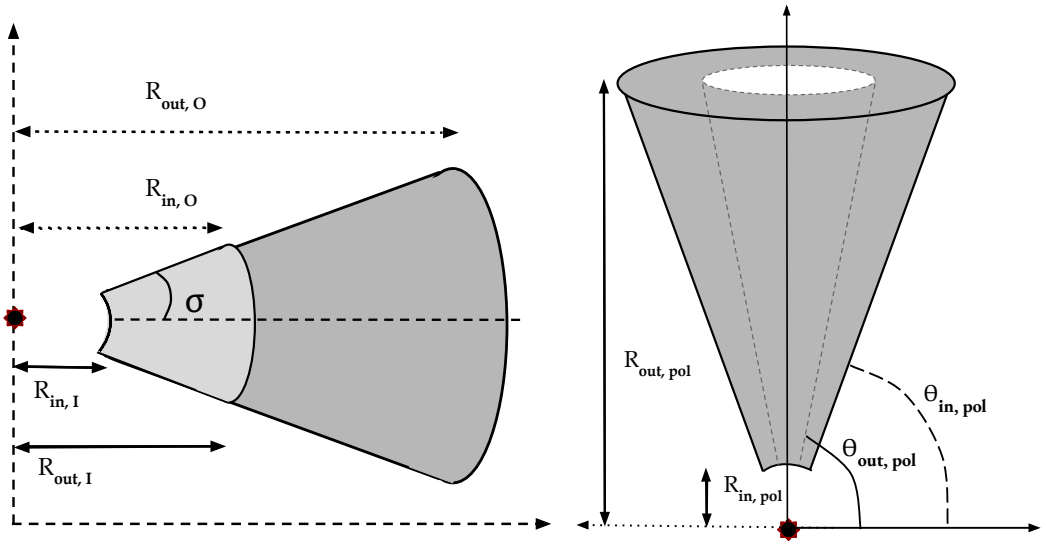


Figure 3. Schematic representation of the structure of a torus. The left diagram shows a two-equatorial torus geometry, and the right figure shows the polar conical shell structure.

The relationship between the $R_{\rm in}$ of the inner torus and the sublimation temperature is given below [74].

$$R_{\rm in} \approx 1.3 \times \sqrt{L_{46}^{AGN}} \cdot T_{1500}^{-2.8}, \quad \text{pc} \tag{1}$$

where L_{46}^{AGN} is the AGN luminosity expressed in 10^{46}erg/s, $T_{1500}^{-2.8}$ is the temperature of the dust mixture in the unit of 1500 K. Considering the value of $R_{\rm in}$ as 0.04 pc, we found that the inner edge of the inner torus has a temperature of ∼1600 K, which is aligned with the results of Lyu and Rieke [62]. The radial extent of the inner torus defines the $R_{\rm in}$ of the outer torus. This was adopted ∼1 pc based on studies by Tristram and Schartmann [75], which found that the warm dust responsible for the mid-IR emission is located about 30 times further outside the dust sublimation radius (30 × 0.04 pc). We also considered the $R_{\rm out}$ of

the torus to be 15 pc aligned with the polarimetric imaging of Ruiz et al. [76] and the earlier radiative transfer modeling works of Swain et al. [50].

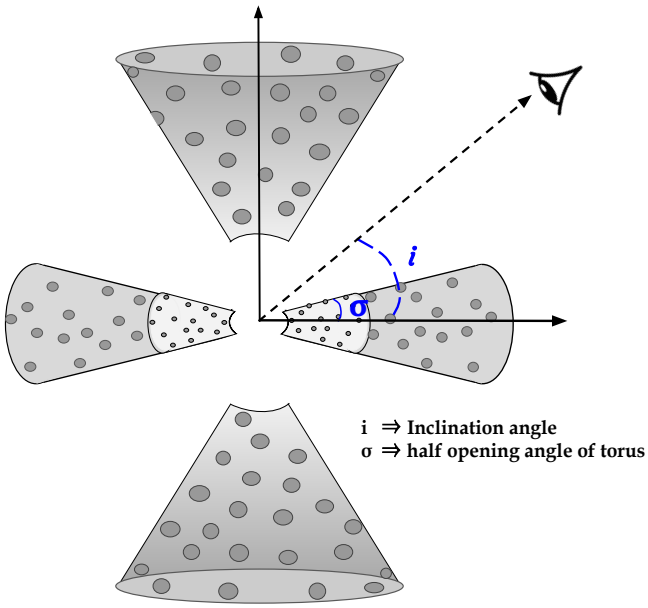


Figure 4. Schematic representation of the equatorial two-torus model with a polar conical shell component. Dimensions are not to scale; the figure is intended for illustration purposes only.

The main parameters for the polar conical shell includes the inner opening angle ($\theta_{\text{in, pol}}$), outer opening angle ($\theta_{\text{out, pol}}$), inner radius ($R_{\text{in, pol}}$), and outer radius ($R_{\text{out, pol}}$), respectively. The direct constraints on the exact angular boundaries of $\theta_{\text{in, pol}}$ and $\theta_{\text{out, pol}}$ are limited. In this work, $\theta_{\text{in, pol}}$ and $\theta_{\text{out, pol}}$ adopted values of 70° and 90°, respectively. These values are broadly consistent with those adopted in earlier studies [22,70].

3.2.1. Dust Composition and Distribution

The spatial dust distribution surrounding the central engine is characterized by a radial dust density power law [77], as shown in Equation (2), that incorporates a density gradient along both the radial (r) and polar (θ) directions.

$$\rho(r, \theta) \propto r^{-p} e^{-q \cos \theta}. \quad (2)$$

Here, p represents the power law index and q represents polar exponent. We adopted a value of 1 for p and 0 for q, as provided by Swain et al. [50].

Dust grains surrounding the AGN must withstand intense radiation from the accretion disk. The silicate and graphite are considered the primary dust components of the AGN torus, with the compositions provided by Draine and Lee [78] (53% silicate and 47% graphite). These distinct silicate and graphite dust grain populations follow the classic Mathis, Rumpl, and Nordsieck (hereby MRN) grain size distribution [79], as given in Equation (3).

$$dN(a) = Ca^{-3.5}\, da, \quad (3)$$

where 'a' denotes the grain size, which takes values between 0.005 µm and 2.5 µm, with normalization factors $C_{\text{Graphite}} = 10^{-15.13}$ and $C_{\text{Silicate}} = 10^{-15.11}$ as taken from Weingartner and Draine [80].

Due to the intense radiation field from the accretion disk of AGNs, small grains may be destroyed. To ensure the survival of smaller dust grains, Krolik and Begelman [10] suggested that dust grains are likely to exist in a clumpy state. Hence, we used a two-phase medium approach, in which high-density clumps were added to a low-density smooth

medium [81]. The parameter clump fraction ($C_{\rm frac}$) provides the fraction of dust mass locked up in clumps.

The clump properties of a torus are primarily described by the total number of clumps ($N_{\rm clumps}$), and the scale radius of each clump ($R_{\rm clump}$). We considered about 1% of the radial extent of the torus as the $R_{\rm clump}$.

The dust is distributed on a three-dimensional Cartesian grid consisting of several cubic cells. Within each cell, the dust density remains uniform. The typical resolution for our simulations is 200 cells per axis. The emission for all models was evaluated using a logarithmically spaced wavelength grid covering the range from 0.005 to 300 µm. An enhanced wavelength resolution was applied between 1 and 20 µm to accurately capture the silicate features. Each simulation utilized 10^8 photon packages (often called photons) for the calculations.

The inclination angle i was adopted as 45° [62,71]. Furthermore, we adopted a distance of 15.8 Mpc to NGC 4151 [26,62].

The volume filling factor ($V_{\rm ff}$) of the torus is the ratio of total volume occupied by the clumps (V_C) to the total volume of the torus (V_T). Earlier works of clumpy/two-phase torus models explored a wide range of volume filling factors ($V_{\rm ff}$), ranging from a very small value, such as ∼0.1%, to even higher than 30% [19,82–85]. López-Gonzaga and Jaffe [83] found that for most of the type-1 objects, the volume filling factors within a 1 pc radius ("inner rim") are between 0.4 and 1.4%. We adopted a $V_{\rm ff}$ value of 0.5% for the inner torus, and 10% for the outer and polar conical shell. The SKIRT input parameter $N_{\rm clumps}$ is derived from the values of $V_{\rm ff}$ and $R_{\rm clump}$. The details of the frozen parameters in the model are presented in Table 2.

Table 2. Values of frozen parameters in our modelling and their references.

Model	Parameter	Adopted Value	Reference
Input SED	L_{Bol}	$5.6 \times 10^9 L_\odot$	
Inner Torus	$R_{\rm in,\,I}$	0.04 pc	Minezaki et al. [72]
	$R_{\rm out,\,I}$	1 pc	
	σ_I	23°	Lyu and Rieke [62]
	$R_{\rm clumps,\,I}$	0.01 pc	
Outer Torus	$R_{\rm in,\,O}$	1 pc	
	$R_{\rm out,\,O}$	15 pc	Swain et al. [50]
	σ_O	23°	Lyu and Rieke [62]
	$R_{\rm clumps,\,O}$	0.14 pc	
Conical Shell	$R_{\rm in,\,pol}$	1 pc	
	$R_{\rm out,\,pol}$	15 pc	
	$\theta_{\rm in,\,pol}$	70°	
	$\theta_{\rm out,\,pol}$	90°	
	$R_{\rm clumps,\,pol}$	0.14 pc	

3.2.2. Estimation of Model Parameters

Input SED model: We varied $T_{\rm in}$ from 3 eV to 10 eV. We found that $T_{\rm in} \geq 6$ eV failed to reproduce the optical/NIR data. However, a $T_{\rm in}$ value of 4–5 eV better explains the observed SED.

Torus model: In our analysis, we vary two torus parameters: (a) the clump fraction ($C_{\rm frac}$) and (b) the optical depth at 9.7 micron ($\tau_{9.7\mu\rm m}$). The wavelength dependence of the optical depth is estimated assuming an MRN dust grain size distribution. The total dust mass within the torus is determined by the parameters p, q, and the optical depth at 9.7 µm ($\tau_{9.7\mu\rm m}$). We adopt the same clump fraction values for all three sub-components of the torus. Our analysis indicates that a higher $C_{\rm frac}$ (0.94–0.95) value for all torus components

is required to reproduce the observed SED. Figure 5 shows the simulated output SED for different values of the clump fraction applied uniformly across all three components.

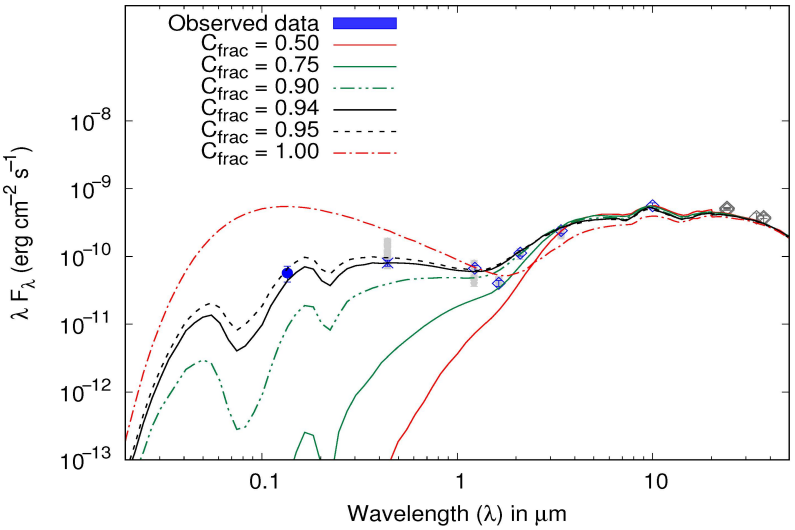


Figure 5. The solid and dashed lines represent model SEDs for different values of clump fraction (C_{frac}) varied for all three components of the torus. The filled blue circles denote the UV data, the blue cross markers represent the optical data points and blue open diamonds denote the NIR data points. The light gray data points in the optical and NIR regime represent the nearest available data within 90 days. Dark gray open diamonds correspond to the non-simultaneous MIR data as obtained from Lyu and Rieke [62]. The optical depths for the inner torus, outer torus, and polar conical shell are fixed at 17, 20, and 20, respectively.

Furthermore, we varied the $\tau_{9.7\mu m}$ of the inner and outer torus and the polar conical shell. We noticed that a higher (>10) value of $\tau_{9.7\mu m}$ for the inner torus is required to explain the observed optical and UV flux. On the other hand, higher values ($\geq$10) of $\tau_{9.7\mu m}$ for the outer torus and polar conical shell are required to explain the observed IR emission. Figure 6 shows the variation of model SED for different values of optical depth.

The salient points of model fittings are summarized below.

- The source has been monitored over a long period in the UV band, and we determined its activity state based on the observed UV flux. Due to limited data points in the SED, we noticed degeneracies in sets of parameter values that provide similar χ^2 values. The optical observations were obtained within a day of the UV measurements. Although IR emission is the most direct tracer of the dusty torus, it is at least a week or more apart from the UV epoch. Further, the observation at 1.63 μm was carried out ∼35 days after the UV observation, and the source was sparsely observed in the waveband around this epoch. There is an overprediction of flux at the H band (1.63 μm) for all sets of model parameters. Table A1 in Appendix A provides the ranges of parameter values with a reduced χ^2 value ranging from 0.9 to 1.1. It is to be noted that the χ^2 values were calculated without considering the 1.63 μm flux.
  Our analysis shows a C_{frac} value of 0.94–0.95 for all torus components and an optical depth in the ranges $\tau_{9.7\mu m,I}$ = 15–20, $\tau_{9.7\mu m,O}$ = 10–25, and $\tau_{9.7\mu m,pol}$ = 10–25 better explain the observed SED. The detailed values of these parameters obtained from the SED modeling are listed in Table 3. Figure 7 represents our model SED for the parameter set T_{in} = 4 eV, C_{frac} = 0.94, $\tau_{9.7\mu m,I}$ = 17, $\tau_{9.7\mu m,O}$ = 20, and $\tau_{9.7\mu m,pol}$ = 20 (reduced χ^2 = 1.04).
- As described in Stalevski et al. [81], for two-phase models comprising both smooth and clumpy components, SKIRT first assigns an optical depth by assuming that the entire medium is smooth. The parameter C_{frac} specifies the fraction of the total dust

mass that is redistributed into clumps. In contrast, the number of clumps and the size of the individual clumps together determine the fraction of the volume occupied by clumps, that is, the volume filling factor. A high value of C_{frac} implies that most of the dust mass resides in clumps, whereas a moderate or low volume filling factor indicates that the medium is predominantly smooth. Our analysis found that the bulk of the dust mass is indeed concentrated in clumps (C_{frac} = 0.94–0.95), while the clumps occupy only a small fraction of the total volume, approximately ∼0.5% in the inner torus and ∼10% in the outer torus and the polar conical shell. Consequently, the optical depth at 9.7 µm associated with the smooth component is expected to be significantly lower than the initially assumed optical depth, whereas the optical depth within individual clumps is expected to be much higher. The effective optical depth along the line of sight, therefore, results from the combined contributions of both components, weighted by their spatial distribution.

- While the non-simultaneous MIR data were not considered for model fitting, they agree with our model predictions (Figure 7).

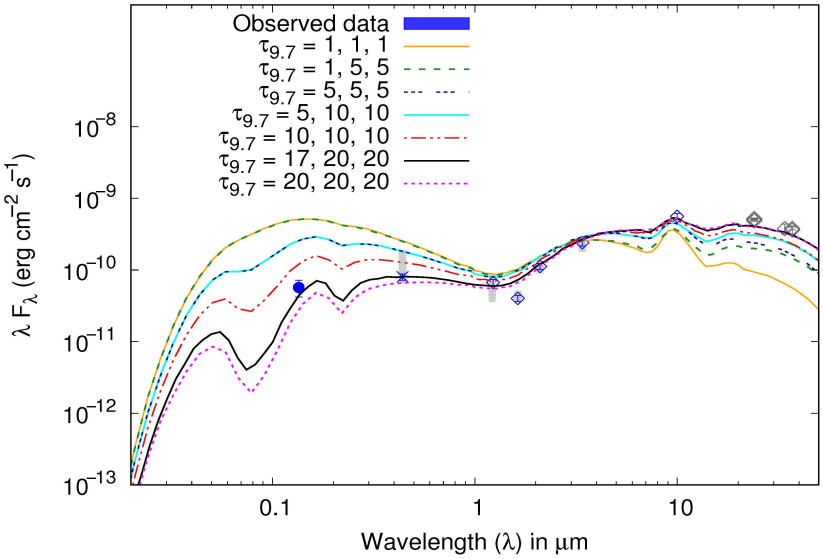


Figure 6. The lines represent model SEDs for different values of optical depth $\tau_{9.7\mu m}$ varied for the inner torus, outer torus, and polar conical shell, respectively. The filled blue circles denote the UV data, the blue cross markers represent the optical data points, and the blue open diamonds denote the NIR data points. The light gray data points in the optical and NIR regimes represent the nearest available data within 90 days. Dark gray open diamonds correspond to the non-simultaneous MIR data as obtained from Lyu and Rieke [62].

Table 3. The explored ranges and the optimum values of the parameters that were varied in modeling.

Model	Parameter	Parameter Range	Final Value
Input SED (diskbb)	T_{in}	3–10 eV	4–5 eV
Inner Torus	$\tau_{9.7\mu m,I}$	0.1–25	15–20
	$N_{clumps,I}$	1954, 3908, 39,071	1954
	$C_{frac,I}$	0.5–1	0.94–0.95
Outer Torus	$\tau_{9.7\mu m,O}$	0.1–25	10–25
	$N_{clumps,O}$	4804, 48,044, 96,088	48,044
	$C_{frac,O}$	0.5–1	0.94–0.95
Conical Shell	$\tau_{9.7\mu m,pol}$	0.1–25	10–25
	$N_{clumps,pol}$	407, 4072, 8144	4072
	$C_{frac,pol}$	0.5–1	0.94–0.95

To examine the effect of the filling factor of different torus components on the model SED, we varied the volume filling factors while the T_{in} and optical depths are kept at their derived values as given in Table 3. Figure 8 shows the variation of the model SED for different volume filling factors. We found that a higher value of V_{ff} for the inner torus could not explain the optical and UV regions, whereas a very low value or very high value of V_{ff} for the outer torus and conical shell can not explain the IR region well.

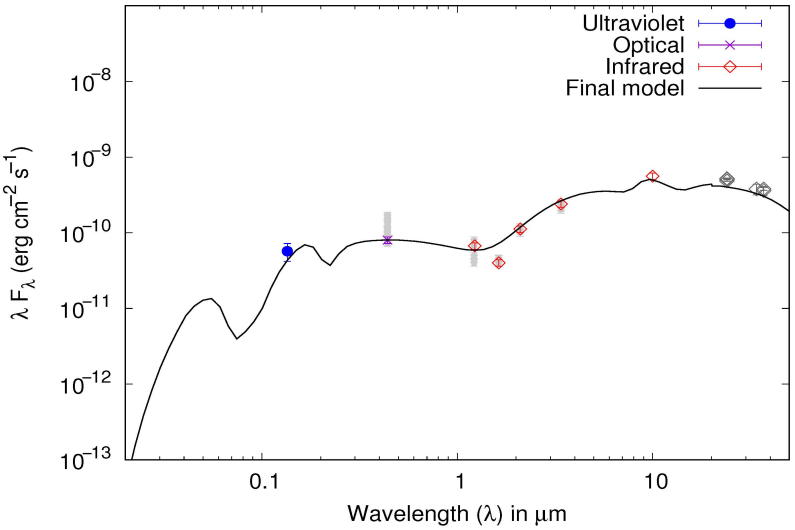


Figure 7. Representative model spectrum along with observed data across the UV, optical, and IR regimes. The model parameter values are T_{in} = 4 eV, C_{frac} = 0.94, $\tau_{9.7\mu m,I}$ = 17, $\tau_{9.7\mu m,O}$ = 20, $\tau_{9.7\mu m,pol}$ = 20, and the reduced χ^2 = 1.04, as shown in Table A1. The filled blue circles denote the UV data, the blue cross markers represent the optical data points, and the blue open diamonds denote the NIR data points. The light gray data points in the optical and NIR regime represent the nearest available data within 90 days. The dark gray open diamonds correspond to the non-simultaneous MIR data as obtained from Lyu and Rieke [62].

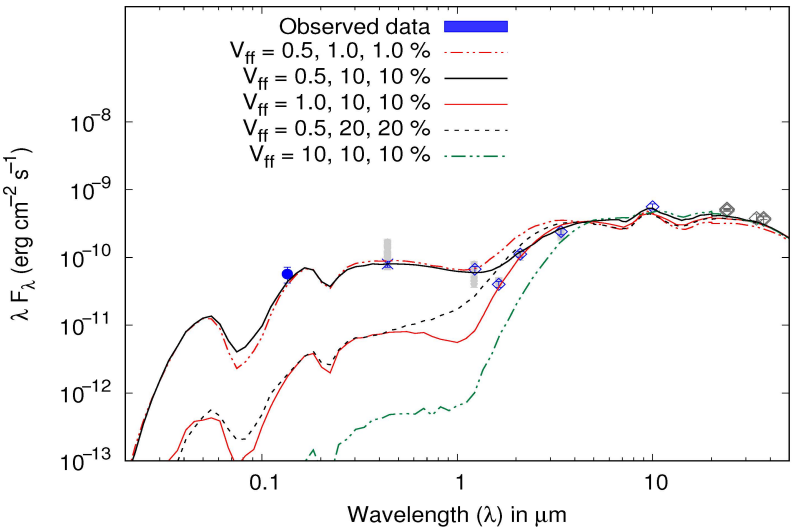


Figure 8. The solid and dashed lines represent model SEDs for different values of volume filling factor (V_{ff}) of the inner torus, outer torus, and polar conical shell, respectively. The filled blue circles denote the UV data, the blue cross markers represent the optical data points, and the blue open diamonds denote the NIR data points. The light gray data points in the optical and NIR regime represent the nearest available data within 90 days. The dark gray open diamonds correspond to the non-simultaneous MIR data as obtained from Lyu and Rieke [62]. The optical depths for the inner torus, outer torus, and polar conical shell are 17, 20, and 20, respectively.

4. Discussions & Conclusions

Given its significant variability and as the brightest nearby AGN, NGC 4151 has been subjected to long-term observations in UV and optical bands. Like other RQ-AGN, earlier studies of this source were restricted to either the IR or the X-ray–UV regime. While there were a few attempts to constrain the torus parameters utilising RT codes, these studies were limited to non-simultaneous IR data collected during various activity states of NGC 4151 [15,20,50,53,86]. Most of these studies employed statistical fitting techniques to estimate the torus parameters (e.g., [15,53]), but the parameters remained poorly constrained due to insufficient data for quantitatively robust model fitting. Furthermore, these studies used average AGN SEDs as input. However, given the intrinsically variable nature of AGN, an average SED may not accurately represent the true spectral energy distribution of a specific source during a particular activity state. In addition, most of these input SEDs were empirically derived, rather than being based on physically motivated models.

In this work, we present the construction and detailed modelling of the near-simultaneous broadband SED of NGC 4151 during one of its UV low states. During March 2000, the source was in one of its historic low activity states. Unlike other low UV activity states, near-simultaneous X-ray, UV, optical, and five IR band observations were available during this epoch. NGC 4151 exhibits complex X-ray emissions, which might have originated from the inner geometrically thick, optically thin disk and/or from the corona. Therefore, we have not explicitly used X-ray data in our modeling. This work represents one of the first comprehensive broadband SED studies conducted on any radio-quiet AGN.

The input SED was derived for a multi-color blackbody spectrum using the `diskbb` model of XSPEC. Since the observations correspond to one of the lowest UV activity states of the source, we adopted an accretion rate of 1% of the Eddington value for NGC 4151 during this period, which is consistent with the observed SED of the source. Notably, the source was in a Type 1.8 state [87] during our study. Our analysis found that a lower accretion rate is consistent with the observed SED.

From the modeling of the broadband SED of NGC 4151, we found that an inner disk temperature of 4–5 eV better explains the observed data. In comparison, Kumar et al. [34], using simultaneous X-ray and UV observations from AstroSat, reported a higher $T_{\rm in}$ value of 9–10 eV that better reproduced their observed SED. It is important to note that their observations correspond to a moderate activity state of the source, whereas our analysis focuses on a low-activity state.

We find that a three-component torus geometry, consisting of (a) two equatorial torus components and (b) a polar conical shell, is essential to reproduce the observed SED. The innermost torus component predominantly influences the UV and optical emissions, whereas the outermost torus and the conical shell have a stronger impact on the IR emissions. The high optical depths obtained in our analysis are consistent with the findings of Swain et al. [50].

Our analysis indicates a high clump fraction (0.94–0.95) for all torus components and a low filling factor (∼0.5%) for the inner torus, while a moderate filling factor (∼10%) is favoured for the outer torus and the polar conical shell. We also find that an inner temperature of the accretion disk in the range $T_{\rm in} \sim$ 4–5 eV, together with high optical depths ($\tau_{9.7\mu m} \geq 10$) across all torus components, is required to satisfactorily reproduce the observed SED. Couto et al. [46] confirm that the 2000 epoch corresponds to a well-defined low-flux state based on both X-ray spectral properties and the long-term UV light curve. The intrinsic N_H value obtained from the X-ray observation is 6×10^{22} cm^{-2}, which suggests that the source has moderate obscuration. This supports the higher optical depth values in the torus components obtained from our analysis.

Additionally, we observe that variations in the model parameters result in more pronounced flux changes in the UV–optical bands than in the infrared. Further, NGC 4151 exhibits strong variability and "changing look" behavior. Future studies using near-simultaneous broadband observations in the UV, optical, and IR regimes, during both low- and high-activity states, will help strengthen our understanding of the accretion disk and torus properties of this source, and may also clarify the physical mechanisms responsible for the changing look behavior in AGN.

Author Contributions: Conceptualization, A.S., D.B., P.S. (Puthiyaveettil Shalima), G.C.D. and P.S. (Parameshwaran Sreekumar); methodology, A.S. and D.B.; formal analysis, A.S.; investigation, A.S., D.B., P.S. (Puthiyaveettil Shalima), G.C.D. and P.S. (Parameshwaran Sreekumar); writing—original draft preparation, A.S. and D.B.; writing—review and editing, A.S., D.B., P.S. (Puthiyaveettil Shalima), G.C.D. and P.S. (Parameshwaran Sreekumar); software, A.S.; visualization, A.S., D.B., P.S. (Puthiyaveettil Shalima), G.C.D. and P.S. (Parameshwaran Sreekumar); supervision, D.B.; project administration, D.B.; funding acquisition, D.B., P.S. (Puthiyaveettil Shalima) and P.S. (Parameshwaran Sreekumar). All authors have read and agreed to the published version of the manuscript.

Funding: This research received no external funding. The APC was funded by Manipal Academy of Higher Education.

Data Availability Statement: The work is based on open data from the literature and publicly available archives and databases. The model SED data will be shared upon reasonable request to the author.

Acknowledgments: We thank the anonymous referees for their valuable comments that helped to improve the quality of the manuscript. The authors thank Mike Crenshaw, Georgia State University, for providing us with the UV data. The authors thank Marko Stalevski, Astronomical Observatory Belgrade, for the fruitful conversations during the initial stages, which clarified the doubts regarding the SKIRT code. We thank Sanna Gulati for helpful suggestions on the manuscript. This research has made use of data and software provided by the HEASARC, which is a service of the Astrophysics Science Division at NASA/GSFC and the High Energy Astrophysics Division of the Smithsonian Astrophysical Observatory. Grammarly 1.2.207 and ChatGPT 5.1 were employed only as a linguistic tool for grammatical corrections, and to polish some sentences for better readability. A.S. acknowledges Dr. TMAPai Ph.D scholarship programme, Manipal Academy of Higher Education (MAHE). Manipal Centre for Natural Sciences, Centre of Excellence, MAHE, is acknowledged for its facilities and support.

Conflicts of Interest: The authors declare no conflicts of interest. The manuscript is approved by all authors for publication.

Appendix A

The reduced χ^2 values obtained in the ranges of 0.9 to 1.1 from SED fitting for different combinations of the inner, outer, and polar dust optical depths are provided in the table below (Table A1).

Table A1. The reduced χ^2 values obtained from SED fitting for different combinations of the inner, outer, and polar dust optical depths. The table lists the input disk temperature ($T_{\rm in}$), clump fraction ($C_{\rm frac}$), optical depths at 9.7 μm for the inner torus ($\tau_{9.7\mu m,I}$), outer torus ($\tau_{9.7\mu m,O}$), and polar dust ($\tau_{9.7\mu m,pol}$), along with the corresponding reduced χ^2.

Sl. No.	$T_{\rm in}$ (eV)	$C_{\rm frac}$	$\tau_{9.7\mu m,I}$	$\tau_{9.7\mu m,O}$	$\tau_{9.7\mu m,pol}$	Reduced-χ^2 (Degrees of Freedom = 5)
1	4	0.94	16	10	10	0.92
2	4	0.94	16	10	15	1.03
3	4	0.94	16	10	20	1.10
4	4	0.94	16	15	15	0.92
5	4	0.94	16	15	20	1.04

Table A1. *Cont.*

Sl. No.	T_{in} (eV)	C_{frac}	$\tau_{9.7\mu m,I}$	$\tau_{9.7\mu m,O}$	$\tau_{9.7\mu m,pol}$	Reduced-χ^2 (Degrees of Freedom = 5)
6	4	0.94	16	20	10	1.05
7	4	0.94	16	20	15	1.05
8	4	0.94	17	10	15	1.10
9	4	0.94	17	15	10	1.06
10	4	0.94	17	15	15	1.02
11	4	0.94	17	20	15	0.98
12	4	0.94	17	20	20	1.04
13	4	0.94	15	25	25	1.06
14	4	0.94	16	16	16	0.93
15	4	0.94	16	16	18	1.03
16	4	0.94	16	16	22	0.96
17	4	0.94	16	16	25	0.99
18	4	0.94	16	18	22	1.01
19	4	0.94	16	22	16	0.98
20	4	0.94	16	22	18	1.08
21	4	0.94	16	22	22	0.98
22	4	0.94	17	16	16	0.91
23	4	0.94	17	16	22	0.91
24	4	0.94	17	16	25	0.96
25	4	0.94	17	18	16	0.90
26	4	0.94	17	18	18	0.90
27	4	0.94	17	18	22	1.00
28	4	0.94	17	18	25	0.98
29	4	0.94	17	22	16	1.03
30	4	0.94	17	22	18	0.96
31	4	0.94	17	22	25	1.01
32	4	0.94	17	25	16	0.97
33	4	0.94	17	25	18	0.92
34	4	0.94	17	25	25	0.94
35	4	0.94	17	20	25	1.09
36	4	0.94	17	25	20	1.08
37	4	0.95	18	10	15	1.03
38	4	0.95	18	10	20	1.07
39	4	0.95	18	15	10	1.10
40	4	0.95	18	15	20	1.04
41	4	0.95	18	20	10	0.92
42	4	0.95	18	20	15	1.07
43	4	0.95	20	15	15	0.94
44	4	0.95	20	20	10	0.97
45	4	0.95	20	20	15	0.90
46	5	0.95	16	10	10	0.91
47	5	0.95	16	10	15	1.03
48	5	0.95	16	10	20	1.10
49	5	0.95	16	15	15	0.91
50	5	0.95	16	15	20	1.04
51	5	0.95	16	20	10	1.05
52	5	0.95	16	20	15	1.04
53	5	0.95	17	10	15	1.10
54	5	0.95	17	15	10	1.05
55	5	0.95	17	15	15	1.01
56	5	0.95	17	20	15	0.98
57	5	0.95	17	20	20	1.04

References

1. Lynden-Bell, D. Galactic Nuclei as Collapsed Old Quasars. *Nature* **1969**, *223*, 690–694. [CrossRef]
2. Kellermann, K.; Sramek, R.; Schmidt, M.; Shaffer, D.; Green, R. VLA observations of objects in the Palomar Bright Quasar Survey. *Astron. J.* **1989**, *98*, 1195–1207. [CrossRef]
3. Schmidt, M.; Green, R.F. Quasar evolution derived from the Palomar bright quasar survey and other complete quasar surveys. *Astrophys. J.* **1983**, *269*, 352–374. [CrossRef]
4. Antonucci, R.R.J.; Miller, J.S. Spectropolarimetry and the nature of NGC 1068. *Astrophys. J.* **1985**, *297*, 621–632. [CrossRef]
5. Urry, C.M.; Padovani, P. Unified schemes for radio-loud active galactic nuclei. *Publ. Astron. Soc. Pac.* **1995**, *107*, 803. [CrossRef]
6. Netzer, H. Revisiting the Unified Model of Active Galactic Nuclei. *Annu. Rev. Astron. Astrophys.* **2015**, *53*, 365–408. [CrossRef]
7. Antonucci, R. Unified models for active galactic nuclei and quasars. *Annu. Rev. Astron. Astrophys.* **1993**, *31*, 473–521. [CrossRef]

8. Pier, E.A.; Krolik, J.H. Infrared Spectra of Obscuring Dust Tori around Active Galactic Nuclei. I. Calculational Method and Basic Trends. *Astrophys. J.* **1992**, *401*, 99. [CrossRef]
9. Fritz, J.; Franceschini, A.; Hatziminaoglou, E. Revisiting the infrared spectra of active galactic nuclei with a new torus emission model. *Mon. Not. R. Astron. Soc.* **2006**, *366*, 767–786. [CrossRef]
10. Krolik, J.H.; Begelman, M.C. Molecular Tori in Seyfert Galaxies: Feeding the Monster and Hiding It. *Astrophys. J.* **1988**, *329*, 702. [CrossRef]
11. Jaffe, W.; Meisenheimer, K.; Röttgering, H.J.A.; Leinert, C.; Richichi, A.; Chesneau, O.; Fraix-Burnet, D.; Glazenborg-Kluttig, A.; Granato, G.L.; Graser, U.; et al. The central dusty torus in the active nucleus of NGC 1068. *Nature* **2004**, *429*, 47–49. [CrossRef] [PubMed]
12. Gordon, K.D.; Misselt, K.A.; Witt, A.N.; Clayton, G.C. The DIRTY Model. I. Monte Carlo Radiative Transfer through Dust. *Astrophys. J.* **2001**, *551*, 269–276. [CrossRef]
13. Dullemond, C.P.; Juhasz, A.; Pohl, A.; Sereshti, F.; Shetty, R.; Peters, T.; Commercon, B.; Flock, M. *RADMC-3D: A Multi-Purpose Radiative Transfer Tool*; Astrophysics Source Code Library: Online, 2012.
14. Camps, P.; Baes, M. SKIRT: An advanced dust radiative transfer code with a user-friendly architecture. *Astron. Comput.* **2015**, *9*, 20–33. [CrossRef]
15. González-Martín, O.; Masegosa, J.; García-Bernete, I.; Ramos Almeida, C.; Rodríguez-Espinosa, J.M.; Márquez, I.; Esparza-Arredondo, D.; Osorio-Clavijo, N.; Martínez-Paredes, M.; Victoria-Ceballos, C.; et al. Exploring the Mid-infrared SEDs of Six AGN Dusty Torus Models. II. The Data. *Astrophys. J.* **2019**, *884*, 11. [CrossRef]
16. Nenkova, M.; Ivezić, Ž.; Elitzur, M. Dust emission from active galactic nuclei. *Astrophys. J.* **2002**, *570*, L9. [CrossRef]
17. Nenkova, M.; Sirocky, M.M.; Ivezić, Ž.; Elitzur, M. AGN dusty tori. I. Handling of clumpy media. *Astrophys. J.* **2008**, *685*, 147. [CrossRef]
18. Hönig, S.F.; Kishimoto, M. The dusty heart of nearby active galaxies. II. From clumpy torus models to physical properties of dust around AGN. *Astron. Astrophys.* **2010**, *523*, A27. [CrossRef]
19. Nenkova, M.; Sirocky, M.M.; Nikutta, R.; Ivezić, Ž.; Elitzur, M. AGN dusty tori. II. Observational implications of clumpiness. *Astrophys. J.* **2008**, *685*, 160. [CrossRef]
20. Siebenmorgen, R.; Heymann, F.; Efstathiou, A. Self-consistent two-phase AGN torus models⋆. SED library for observers. *Astron. Astrophys.* **2015**, *583*, A120. [CrossRef]
21. Stalevski, M.; Ricci, C.; Ueda, Y.; Lira, P.; Fritz, J.; Baes, M. The dust covering factor in active galactic nuclei. *Mon. Not. R. Astron. Soc.* **2016**, *458*, 2288–2302. [CrossRef]
22. Hönig, S.F.; Kishimoto, M. Dusty winds in active galactic nuclei: Reconciling observations with models. *Astrophys. J. Lett.* **2017**, *838*, L20. [CrossRef]
23. Stalevski, M.; Asmus, D.; Tristram, K.R.W. Dissecting the active galactic nucleus in Circinus—I. Peculiar mid-IR morphology explained by a dusty hollow cone. *Mon. Not. R. Astron. Soc.* **2017**, *472*, 3854–3870. [CrossRef]
24. Isbell, J.W.; Meisenheimer, K.; Pott, J.U.; Stalevski, M.; Tristram, K.R.W.; Sanchez-Bermudez, J.; Hofmann, K.H.; Gámez Rosas, V.; Jaffe, W.; Burtscher, L.; et al. The dusty heart of Circinus. I. Imaging the circumnuclear dust in N-band. *Astron. Astrophys.* **2022**, *663*, A35. [CrossRef]
25. de Vaucouleurs, G.; de Vaucouleurs, A.; Corwin, H.G., Jr.; Buta, R.J.; Paturel, G.; Fouque, P. *Third Reference Catalogue of Bright Galaxies*; Springer: Berlin/Heidelberg, Germany, 1991.
26. Yuan, W.; Fausnaugh, M.M.; Hoffmann, S.L.; Macri, L.M.; Peterson, B.M.; Riess, A.G.; Bentz, M.C.; Brown, J.S.; Bontà, E.D.; Davies, R.I.; et al. The Cepheid Distance to the Seyfert 1 Galaxy NGC 4151. *Astrophys. J.* **2020**, *902*, 26. [CrossRef]
27. Khachikian, E.Y.; Weedman, D.W. An atlas of Seyfert galaxies. *Astrophys. J.* **1974**, *192*, 581–589. [CrossRef]
28. Kishimoto, M.; Hönig, S.F.; Antonucci, R.; Barvainis, R.; Kotani, T.; Tristram, K.R.W.; Weigelt, G.; Levin, K. The innermost dusty structure in active galactic nuclei as probed by the Keck interferometer. *Astron. Astrophys.* **2011**, *527*, A121. [CrossRef]
29. Oknyanskii, V.L.; Lyutyi, V.M.; Chuvaev, K.K. NGC4151 after the Deep Minimum of 1984. *Sov. Astron. Lett.* **1991**, *17*, 100.
30. Crenshaw, D.M.; Kraemer, S.B. Mass Outflow from the Nucleus of the Seyfert 1 Galaxy NGC 4151. *Astrophys. J.* **2007**, *659*, 250–256. [CrossRef]
31. Li, S.S.; Feng, H.C.; Liu, H.T.; Bai, J.M.; Li, R.; Lu, K.X.; Wang, J.G.; Huang, Y.K.; Zhang, Z.X. Velocity-resolved Reverberation Mapping of Changing-look Active Galactic Nucleus NGC 4151 during Outburst Stage: Evidence for Kinematics Evolution of Broad-line Region. *Astrophys. J.* **2022**, *936*, 75. [CrossRef]
32. Mahmoud, R.D.; Done, C. Discarding the disc in a changing-state AGN: The UV/X-ray relation in NGC 4151. *Mon. Not. R. Astron. Soc.* **2020**, *491*, 5126–5139. [CrossRef]
33. Feng, H.C.; Li, S.S.; Bai, J.M.; Liu, H.T.; Lu, K.X.; Pang, Y.X.; Sun, M.; Wang, J.G.; Zhang, Y.W.; Zhou, S. Velocity-resolved Reverberation Mapping of Changing-look Active Galactic Nucleus NGC 4151 during Outburst Stage. II. Four Season Observation Results. *arXiv* **2024**, arXiv:2409.01637. [CrossRef]

34. Kumar, S.; Dewangan, G.C.; Gandhi, P.; Papadakis, I.E.; Mithun, N.P.S.; Singh, K.P.; Bhattacharya, D.; Zdziarski, A.A.; Stewart, G.C.; Bhattacharyya, S.; et al. Multi-epoch UV–X-ray spectral study of NGC 4151 with AstroSat. *arXiv* **2024**, arXiv:2409.04762. [CrossRef]
35. Rudnick, L.; Sitko, M.L.; Stein, W.A. The nature of radio-quiet QSO's VLA observations of 0026+129, 0205+024 and 1351+640. *Astron. J.* **1984**, *89*, 753–757. [CrossRef]
36. Mundell, C.G.; Wrobel, J.M.; Pedlar, A.; Gallimore, J.F. The Nuclear Regions of the Seyfert Galaxy NGC 4151: Parsec-Scale H I Absorption and a Remarkable Radio Jet. *Astrophys. J.* **2003**, *583*, 192–204. [CrossRef]
37. Wang, J.; Fabbiano, G.; Karovska, M.; Elvis, M.; Risaliti, G.; Zezas, A.; Mundell, C.G. The Highest Resolution Chandra View of Photoionization and Jet-Cloud Interaction in the Nuclear Region of NGC 4151. *Astrophys. J.* **2009**, *704*, 1195–1203. [CrossRef]
38. Williams, D.R.A.; McHardy, I.M.; Baldi, R.D.; Beswick, R.J.; Argo, M.K.; Dullo, B.T.; Knapen, J.H.; Brinks, E.; Fenech, D.M.; Mundell, C.G.; et al. Radio jets in NGC 4151: Where eMERLIN meets HST. *Mon. Not. R. Astron. Soc.* **2017**, *472*, 3842–3853. [CrossRef]
39. Williams, D.R.A.; Baldi, R.D.; McHardy, I.M.; Beswick, R.J.; Panessa, F.; May, D.; Moldón, J.; Argo, M.K.; Bruni, G.; Dullo, B.T.; et al. The curious activity in the nucleus of NGC 4151: Jet interaction causing variability? *Mon. Not. R. Astron. Soc.* **2020**, *495*, 3079–3086. [CrossRef]
40. Peretti, E.; Peron, G.; Tombesi, F.; Lamastra, A.; Saturni, F.G.; Cerruti, M.; Ahlers, M. Gamma-ray emission from the Seyfert galaxy NGC 4151: Multi-messenger implications for ultra-fast outflows. *J. Cosmol. Astropart. Phys.* **2025**, *2025*, 13. [CrossRef]
41. Inoue, Y.; Khangulyan, D. Gamma-ray emission in the Seyfert galaxy NGC 4151: Investigating the role of jet and coronal activities. *Publ. Astron. Soc. Jpn.* **2023**, *75*, L33–L39. [CrossRef]
42. Ricci, C.; Trakhtenbrot, B. Changing-look active galactic nuclei. *Nat. Astron.* **2023**, *7*, 1282–1294. [CrossRef]
43. Oknyanskij, V.L.; Metlova, N.V.; Huseynov, N.A.; Guo, D.F.; Lyuty, V.M. Optical Monitoring of NGC4151 During 110 Years. *Odessa Astron. Publ.* **2016**, *29*, 95. [CrossRef]
44. Crenshaw, D.M.; Rodriguez-Pascual, P.M.; Penton, S.V.; Edelson, R.A.; Alloin, D.; Ayres, T.R.; Clavel, J.; Horne, K.; Johnson, W.N.; Kaspi, S.; et al. Multiwavelength Observations of Short-Timescale Variability in NGC 4151. I. Ultraviolet Observations. *Astrophys. J.* **1996**, *470*, 322. [CrossRef]
45. Penston, M.V.; Boksenberg, A.; Bromage, G.E.; Clavel, J.; Elvius, A.; Gondhalekar, P.M.; Jordan, C.; Lind, J.; Lindegren, L.; Perola, G.C.; et al. Detailed observations of NGC 4151 with the IUE. I. Low dispersion data up to 1979 january. *Mon. Not. R. Astron. Soc.* **1981**, *196*, 857–887. [CrossRef]
46. Couto, J.D.; Kraemer, S.B.; Turner, T.J.; Crenshaw, D.M. New Insights into the Spectral Variability and Physical Conditions of the X-Ray Absorbers in NGC 4151. *Astrophys. J.* **2016**, *833*, 191. [CrossRef]
47. Lyu, J.; Rieke, G. Infrared Spectral Energy Distribution and Variability of Active Galactic Nuclei: Clues to the Structure of Circumnuclear Material. *Universe* **2022**, *8*, 304. [CrossRef]
48. Koshida, S.; Yoshii, Y.; Kobayashi, Y.; Minezaki, T.; Sakata, Y.; Sugawara, S.; Enya, K.; Suganuma, M.; Tomita, H.; Aoki, T.; et al. Variation of Inner Radius of Dust Torus in NGC4151. *Astrophys. J.* **2009**, *700*, L109–L113. [CrossRef]
49. Hönig, S.F.; Kishimoto, M. Constraining properties of dusty environments by infrared variability. *Astron. Astrophys.* **2011**, *534*, A121. [CrossRef]
50. Swain, S.; Shalima, P.; Latha, K.V.P.; Swamy, K.B.S. Hot graphite dust in the inner regime of NGC 4151. *Mon. Not. R. Astron. Soc.* **2021**, *503*, 5877–5893. [CrossRef]
51. Edelson, R.A.; Alexander, T.; Crenshaw, D.M.; Kaspi, S.; Malkan, M.A.; Peterson, B.M.; Warwick, R.S.; Clavel, J.; Filippenko, A.V.; Horne, K.; et al. Multiwavelength Observations of Short-Timescale Variability in NGC 4151. IV. Analysis of Multiwavelength Continuum Variability. *Astrophys. J.* **1996**, *470*, 364. [CrossRef]
52. Yang, Y.; Wilson, A.S.; Ferruit, P. Chandra X-Ray Observations of NGC 4151. *Astrophys. J.* **2001**, *563*, 124–134. [CrossRef]
53. Ramos Almeida, C.; Levenson, N.A.; Rodríguez Espinosa, J.M.; Alonso-Herrero, A.; Asensio Ramos, A.; Radomski, J.T.; Packham, C.; Fisher, R.S.; Telesco, C.M. The Infrared Nuclear Emission of Seyfert Galaxies on Parsec Scales: Testing the Clumpy Torus Models. *Astrophys. J.* **2009**, *702*, 1127–1149. [CrossRef]
54. Alonso-Herrero, A.; Ramos Almeida, C.; Mason, R.; Asensio Ramos, A.; Roche, P.F.; Levenson, N.A.; Elitzur, M.; Packham, C.; Rodríguez Espinosa, J.M.; Young, S.; et al. Torus and Active Galactic Nucleus Properties of Nearby Seyfert Galaxies: Results from Fitting Infrared Spectral Energy Distributions and Spectroscopy. *Astrophys. J.* **2011**, *736*, 82. [CrossRef]
55. Alonso-Herrero, A.; Quillen, A.C.; Rieke, G.H.; Ivanov, V.D.; Efstathiou, A. Spectral Energy Distributions of Seyfert Nuclei. *Astron. J.* **2003**, *126*, 81–100. [CrossRef]
56. Cerqueira-Campos, F.C.; Rodríguez-Ardila, A.; Panda, S.; Riffel, R.; Dahmer-Hahn, L.G.; Marinello, M. Coronal line forest AGN—II. Analysis of the spectral energy distribution. *Mon. Not. R. Astron. Soc.* **2023**, *524*, 542–554. [CrossRef]
57. Marin, F.; Marinucci, A.; Laurenti, M.; Kim, D.E.; Barnouin, T.; Di Marco, A.; Ursini, F.; Bianchi, S.; Ravi, S.; Marshall, H.L.; et al. X-ray polarization measurement of the gold standard of radio-quiet active galactic nuclei: NGC 1068. *arXiv* **2024**, arXiv:2403.02061. [CrossRef]

58. Bhattacharya, D.; Misra, R.; Rao, A.R.; Sreekumar, P. The uncorrelated long-term γ-ray and X-ray variability of blazars and its implications on disc-jet coupling. *Mon. Not. R. Astron. Soc.* **2013**, *431*, 1618–1624. [CrossRef]
59. Bhattacharya, D.; Mohana A, K.; Bhattacharyya, S.; Bhatt, N.; Stalin, C.S. Multiwavelength study of different flaring and low-activity states of blazar 4C+21.35. *Mon. Not. R. Astron. Soc.* **2021**, *500*, 1127–1138. [CrossRef]
60. Kraemer, S.B.; Crenshaw, D.M.; Gabel, J.R.; Kriss, G.A.; Netzer, H.; Peterson, B.M.; George, I.M.; Gull, T.R.; Hutchings, J.B.; Mushotzky, R.F.; et al. Simultaneous Ultraviolet and X-Ray Observations of the Seyfert Galaxy NGC 4151. II. Physical Conditions in the UV Absorbers. *Astrophys. J. Suppl. Ser.* **2006**, *167*, 161–176. [CrossRef]
61. Lyu, J.; Rieke, G.H. B and JHKL Light Curves of NGC 4151 VizieR Online Data Catalog: J/ApJ/912/126. 2021. Available online: https://cdsarc.cds.unistra.fr/viz-bin/cat/J/ApJ/912/126 (accessed on 16 June 2025).
62. Lyu, J.; Rieke, G.H. The Dusty Heart of NGC 4151 Revealed by $\lambda \sim$ 1–40 µm Reverberation Mapping and Variability: A Challenge to Current Clumpy Torus Models. *Astrophys. J.* **2021**, *912*, 126. [CrossRef]
63. Gorjian, V.; Werner, M.W.; Jarrett, T.H.; Cole, D.M.; Ressler, M.E. 10 Micron Imaging of Seyfert Galaxies from the 12 Micron Sample. *Astrophys. J.* **2004**, *605*, 156–167. [CrossRef]
64. Camps, P.; Baes, M. SKIRT 9: Redesigning an advanced dust radiative transfer code to allow kinematics, line transfer and polarization by aligned dust grains. *Astron. Comput.* **2020**, *31*, 100381. [CrossRef]
65. Schartmann, M.; Meisenheimer, K.; Camenzind, M.; Wolf, S.; Henning, T. Towards a physical model of dust tori in Active Galactic Nuclei-Radiative transfer calculations for a hydrostatic torus model. *Astron. Astrophys.* **2005**, *437*, 861–881. [CrossRef]
66. Feltre, A.; Hatziminaoglou, E.; Fritz, J.; Franceschini, A. Smooth and clumpy dust distributions in AGN: A direct comparison of two commonly explored infrared emission models. *Mon. Not. R. Astron. Soc.* **2012**, *426*, 120–127. [CrossRef]
67. Bentz, M.C.; Williams, P.R.; Treu, T. The Broad Line Region and Black Hole Mass of NGC 4151. *Astrophys. J.* **2022**, *934*, 168. [CrossRef]
68. Radomski, J.T.; Piña, R.K.; Packham, C.; Telesco, C.M.; Buizer, J.M.D.; Fisher, R.S.; Robinson, A. Resolved Mid-Infrared Emission in the Narrow-Line Region of NGC 4151. *Astrophys. J.* **2003**, *587*, 117. [CrossRef]
69. Asmus, D. New evidence for the ubiquity of prominent polar dust emission in AGN on tens of parsec scales. *Mon. Not. R. Astron. Soc.* **2019**, *489*, 2177–2188. [CrossRef]
70. Swain, S.; Shalima, P.; Latha, K.V.P. Unravelling the nuclear dust morphology of NGC 1365: A two-phase polar-RAT model for the ultraviolet to infrared spectral energy distribution. *Mon. Not. R. Astron. Soc.* **2024**, *527*, 3592–3601. [CrossRef]
71. Das, V.; Crenshaw, D.M.; Hutchings, J.B.; Deo, R.P.; Kraemer, S.B.; Gull, T.R.; Kaiser, M.E.; Nelson, C.H.; Weistrop, D. Mapping the Kinematics of the Narrow-Line Region in the Seyfert Galaxy NGC 4151. *Astron. J.* **2005**, *130*, 945–956. [CrossRef]
72. Minezaki, T.; Yoshii, Y.; Kobayashi, Y.; Enya, K.; Suganuma, M.; Tomita, H.; Aoki, T.; Peterson, B.A. Inner Size of a Dust Torus in the Seyfert 1 Galaxy NGC 4151. *Astrophys. J.* **2003**, *600*, L35. [CrossRef]
73. Kishimoto, M.; Hönig, S.F.; Antonucci, R.; Kotani, T.; Barvainis, R.; Tristram, K.R.W.; Weigelt, G. Exploring the inner region of type 1 AGNs with the Keck interferometer. *Astron. Astrophys.* **2009**, *507*, L57–L60. [CrossRef]
74. Barvainis, R. Hot dust and the near-infrared bump in the continuum spectra of quasars and active galactic nuclei. *Astrophys. J.* **1987**, *320*, 537–544. [CrossRef]
75. Tristram, K.R.W.; Schartmann, M. On the size-luminosity relation of AGN dust tori in the mid-infrared. *Astron. Astrophys.* **2011**, *531*, A99. [CrossRef]
76. Ruiz, M.; Young, S.; Packham, C.; Alexander, D.M.; Hough, J.H. Near-infrared imaging polarimetry and modelling of NGC 4151. *Mon. Not. R. Astron. Soc.* **2003**, *340*, 733–738. [CrossRef]
77. Granato, G.; Danese, L. Thick tori around active galactic nuclei: A comparison of model predictions with observations of the infrared continuum and silicate features. *Mon. Not. R. Astron. Soc.* **1994**, *268*, 235–252. [CrossRef]
78. Draine, B.T.; Lee, H.M. Optical Properties of Interstellar Graphite and Silicate Grains. *Astrophys. J.* **1984**, *285*, 89. [CrossRef]
79. Mathis, J.S.; Rumpl, W.; Nordsieck, K.H. The size distribution of interstellar grains. *Astrophys. J.* **1977**, *217*, 425–433. [CrossRef]
80. Weingartner, J.C.; Draine, B.T. Dust Grain-Size Distributions and Extinction in the Milky Way, Large Magellanic Cloud, and Small Magellanic Cloud. *Astrophys. J.* **2001**, *548*, 296–309. [CrossRef]
81. Stalevski, M.; Fritz, J.; Baes, M.; Nakos, T.; Popović, L.Č. 3D radiative transfer modelling of the dusty tori around active galactic nuclei as a clumpy two-phase medium. *Mon. Not. R. Astron. Soc.* **2012**, *420*, 2756–2772. [CrossRef]
82. Elitzur, M.; Shlosman, I. The AGN-obscuring Torus: The End of the "Doughnut" Paradigm? *Astrophys. J.* **2006**, *648*, L101–L104. [CrossRef]
83. López-Gonzaga, N.; Jaffe, W. Mid-infrared interferometry of Seyfert galaxies: Challenging the Standard Model. *Astron. Astrophys.* **2016**, *591*, A128. [CrossRef]
84. Hönig, S.F. Tori, Discs, and Winds: The First Ten Years of AGN Interferometry. In *Astronomy at High Angular Resolution*; Boffin, H.M.J., Hussain, G., Berger, J.P., Schmidtobreick, L., Eds.; Springer: Berlin/Heidelberg, Germany, 2016; Volume 439, p. 95. [CrossRef]

85. Vollmer, B.; Davies, R.I.; Gratier, P.; Lizée, T.; Imanishi, M.; Gallimore, J.F.; Impellizzeri, C.M.V.; García-Burillo, S.; Le Petit, F. From the Circumnuclear Disk in the Galactic Center to thick, obscuring tori of AGNs. Modeling the molecular emission of a parsec-scale torus as found in NGC 1068. *Astron. Astrophys.* **2022**, *665*, A102. [CrossRef]
86. Ramos Almeida, C.; Levenson, N.A.; Alonso-Herrero, A.; Asensio Ramos, A.; Rodríguez Espinosa, J.M.; Pérez García, A.M.; Packham, C.; Mason, R.; Radomski, J.T.; Díaz-Santos, T. Testing the Unification Model for Active Galactic Nuclei in the Infrared: Are the Obscuring Tori of Type 1 and 2 Seyferts Different? *Astrophys. J.* **2011**, *731*, 92. [CrossRef]
87. Shapovalova, A.I.; Popović, L.Č.; Collin, S.; Burenkov, A.N.; Chavushyan, V.H.; Bochkarev, N.G.; Benítez, E.; Dultzin, D.; Kovačević, A.; Borisov, N.; et al. Long-term variability of the optical spectra of NGC 4151— I. Light curves and flux correlations. *Astron. Astrophys.* **2008**, *486*, 99–111. [CrossRef]

Disclaimer/Publisher's Note: The statements, opinions and data contained in all publications are solely those of the individual author(s) and contributor(s) and not of MDPI and/or the editor(s). MDPI and/or the editor(s) disclaim responsibility for any injury to people or property resulting from any ideas, methods, instructions or products referred to in the content.